Available online at www.sciencedirect.com

ScienceDirect

Geochimica et Cosmochimica Acta 265 (2019) 19–31

Geochimica et Cosmochimica Acta

www.elsevier.com/locate/gca

Cosmogenic ^{3}He production rate in ilmenite and the redistribution of spallation ^{3}He in fine-grained minerals

Isaac J. Larsen [a,*], Kenneth A. Farley [b], Michael P. Lamb [b]

[a] Department of Geosciences, University of Massachusetts, Amherst, MA 01003, USA
[b] Division of Geological and Planetary Sciences, California Institute of Technology, Pasadena, CA 91125, USA

Received 22 January 2019; accepted in revised form 19 August 2019; Available online 26 August 2019

Abstract

Cosmogenic nuclide surface exposure dating and erosion rate measurements in basaltic landscapes rely primarily on measurement of ^{3}He in olivine or pyroxene. However, geochemical investigations using ^{3}He have been impossible in the substantial fraction of basalts that lack separable olivine or pyroxene crystals, or where such crystals were present, but have been chemically weathered. Fine-textured basalts often contain small grains of ilmenite, a weathering-resistant mineral that is a target for cosmogenic ^{3}He production with good He retention and straightforward mineral separation, but with a poorly constrained production rate. Here we empirically calibrate the cosmogenic ^{3}He production rate in ilmenite by measuring ^{3}He concentrations in basalts with fine-grained (~20 μm cross-section) ilmenite and co-existing pyroxene or olivine from the Columbia River and Snake River Plain basalt provinces in the western United States. The concentration ratio of ilmenite to pyroxene and olivine is 0.78 ± 0.02, yielding an apparent cosmogenic ^{3}He production rate of 93.6 ± 7.7 atom g^{-1} yr^{-1} that is 20–30% greater than expected from prior theoretical and empirical estimates for compositionally similar minerals. The production rate discrepancy arises from the high energy with which cosmic ray spallation reactions emit tritium and ^{3}He and the associated long stopping distances that cause them to redistribute within a rock. Fine-grained phases with low cosmogenic ^{3}He production rates, like ilmenite, will have anomalously high production rates owing to net implantation of ^{3}He from the surrounding, higher ^{3}He production rate, matrix. Semi-quantitative modeling indicates implantation of spallation ^{3}He increases with decreasing ilmenite grain size, leading to production rates that exceed those in a large grain by ~10% when grain radii are <150 μm. The modeling predicts that for the ilmenite grain size in our samples, implantation causes production rates to be ~20% greater than expected for a large grain, and within uncertainty resolves the discrepancy between our calibrated production rate, theory, and rates from previous work. The redistribution effect is maximized when the host rock and crystals differ substantially in mean atomic number, as they do between whole-rock basalt and ilmenite.

Keywords: Cosmogenic nuclide production rate; Ilmenite; Spallation; ^{3}He; Basalt

1. INTRODUCTION

Cosmogenic ^{3}He is a stable noble gas useful for investigating a wide range of Earth surface processes (Cerling and Craig, 1994, Niedermann, 2002). For example, ^{3}He concentrations have been used to determine exposure dates for mass wasting deposits (Cerling, et al., 1999, Marchetti and Cerling, 2005, Mackey and Quigley, 2014), glacial moraines (Licciardi et al., 2001, Blard et al., 2007, Bromley et al., 2011), lava flows (Laughlin, et al., 1994, Fenton and Niedermann, 2014) and fluvially-eroded bedrock (Cerling et al., 1994, Ruszkiczay-Rüdiger et al., 2005, Mackey et al., 2014, Lamb et al., 2014, Baynes et al.,

* Corresponding author.
E-mail addresses: ilarsen@umass.edu (I.J. Larsen), farley@gps.caltech.edu (K.A. Farley), mpl@gps.caltech.edu (M.P. Lamb).

https://doi.org/10.1016/j.gca.2019.08.025
0016-7037/

2015), and to quantify erosion rates (Craig and Poreda, 1986, Gayer et al., 2008, Ferrier et al., 2013). Exposure dating and measurements of erosion rates with ^{3}He typically take place in landscapes with volcanic bedrock that contains olivine or pyroxene phenocrysts, which quantitatively retain He at Earth surface conditions (Hart 1984, Trull et al., 1991) and are relatively easy to separate from the host rock (Cerling, 1990). Because of the utility of ^{3}He for exposure dating, much effort has been devoted to determining the ^{3}He production rate in olivine and pyroxene, usually via measurements on independently dated lava flows (Kurz et al., 1990, Cerling and Craig, 1994, Licciardi et al., 1999, Ackert et al., 2003, Dunai and Wijbrans, 2000, Goehring, et al., 2010, Blard et al., 2013). Such calibration data suggest the ^{3}He production rates in olivine and pyroxene are similar, and, scaled to sea level and high latitude (Lal 1991, Stone 2000), are both approximately 120 atoms g^{-1} yr^{-1} (Goehring et al., 2010, Martin et al., 2017).

To expand the range of rock types that can be dated with ^{3}He, several studies have calibrated the ^{3}He production rate in additional minerals, which typically involves determining the concentration ratio of ^{3}He in the new mineral against that in minerals with well-established production rates, such as ^{10}Be and ^{21}Ne in quartz or ^{3}He in olivine or pyroxene (Kober et al., 2005, Amidon et al., 2009, Shuster et al., 2012). In this way ^{3}He production rates have been estimated for garnet (Gayer, et al., 2004, Amidon, et al., 2008, Amidon et al., 2009), zircon and apatite (Farley et al., 2006, Amidon et al., 2008, Amidon et al., 2009, Amidon and Farley, 2011), biotite and hornblende (Amidon and Farley, 2012), hematite (Shuster et al., 2012) and magnetite-ilmenite mixtures (Kober et al., 2005).

Ilmenite is a common accessory mineral in igneous, metamorphic, and sedimentary rocks (Force, 1991) and is very resistant to chemical weathering (Goldich, 1938). Hence ilmenite could be used for exposure dating and to quantify erosion rates where minerals that are more commonly analyzed for cosmogenic nuclides are absent or have been altered by chemical weathering such that they are unsuitable for analysis. In basaltic landscapes with tropical climates, for example, olivine dissolves in the weathering zone, which causes a spatially un-representative contribution of olivine to stream sediment, hindering the interpretation of ^{3}He concentrations as erosion rates (Ferrier et al., 2013, Mackey et al., 2014), whereas ^{3}He measured in ilmenite would more robustly reflect catchment-averaged erosion.

Ilmenite is isostructural with hematite and differs only in the substitution of a Ti atom for one of the Fe atoms. Previous work has shown that hematite is extremely He retentive (Farley, 2018), and it can be reasonably inferred that ilmenite is as well. Hence if its cosmogenic ^{3}He production rate can be well-constrained, there is potential for ilmenite to be used for a wide range of geological applications. Importantly, the production rate of ^{3}He in stoichiometric ilmenite should be very similar to that of hematite because the production rate from Ti and Fe, neighbors on the periodic table, should be similar (Masarik and Reedy, 1996). There have been only a few attempts at ^{3}He production rate calibration of Fe-Ti oxide phases, and the inferred production rates among these studies vary considerably. For example, measurement of ^{3}He in Fe-Ti oxide minerals with magnetite and ilmenite composition and ^{21}Ne in quartz from an ignimbrite in northern Chile suggest a high production rate of 120 ± 12 atoms g^{-1} yr^{-1} (Kober et al., 2005). In contrast, measurement of ^{3}He in coexisting ilmenite and pyroxene from two Ferrar dolerite boulders in the Dry Valleys, Antarctica indicate production rates in ilmenite are 35–40% lower than in pyroxene (Margerison et al., 2005), or 72–78 atoms g^{-1} yr^{-1}. Similarly, calibration of ^{3}He production rates in hematite against ^{21}Ne in quartz from samples in Brazil indicate a lower production rate of 68.1 ± 8.1 atoms g^{-1} yr^{-1} (Shuster et al., 2012), which is comparable to a theoretically-predicted production rate of 67 atoms g^{-1} yr^{-1} (Masarik and Reedy, 1996). Hence, prior work indicates the cosmogenic ^{3}He production rate in ilmenite should be on the order of 70 atoms g^{-1} yr^{-1}, with the exception of the results of Kober et al. (2005) that suggest rates 70% greater.

Here we use ^{3}He concentrations in ilmenite and coexisting pyroxene or olivine from two volcanic provinces in the western U.S. to calibrate the ^{3}He production rate in ilmenite. The production rate we obtain is greater than expected from hematite (Shuster et al, 2012), as discussed in Section 3. In Section 4, we investigated whether this discrepancy could arise from redistribution of spalled ^{3}He and ^{3}H (tritium), in much the same way that energetic α particles (Farley et al., 1996) and Li-produced ^{3}He (Dunai et al., 2007) are redistributed. Modeling confirms a major role for redistribution of spallation ^{3}He, with a net influx of ^{3}He into fine-grained ilmenite.

2. METHODS

2.1. Samples and analyses

We used samples for He isotope measurement from two locations with basalt bedrock in the western United States, the Miocene age Columbia River Basalt Group in eastern Washington (Barry et al., 2013) and the Pliocene-Holocene age Snake River Plain basalts in Idaho (Tauxe et al., 2004). We measured He isotope abundances in 19 samples, 14 from the Columbia River Basalt, and 5 from the Snake River Plain (Table 1). The samples from Washington were collected from the Priest Rapids, Roza, and Frenchman Springs Members of the Wanapum Basalt Formation from eroded bedrock surfaces scoured by Pleistocene mega-floods or from flood transported boulders (Bretz, 1923). The samples from the Snake River Plain were from the Gooding Butte basalt and ^{3}He was previously measured in olivine from these samples for exposure dating of fluvially-eroded bedrock (Lamb et al., 2014). The Columbia River Basalt Group members we sampled do not contain olivine or pyroxene phenocrysts that are typically used for ^{3}He exposure dating but do contain small ilmenite and pyroxene crystals within the groundmass. Ilmenite was separated from most samples, and pyroxene was successfully separated from a smaller subset of the samples. Hence we used the samples with both ilmenite and pyroxene to calibrate the ^{3}He production rate in ilmenite for future exposure dating of samples where only ilmenite

Table 1
Helium isotope abundance data.

Sample ID	Mass (g)	^{3}He (10^6 at g^{-1})	^{3}He 1σ SD (10^6 at g^{-1})	^{4}He (10^{-9} cc STP g^{-1})	^{4}He 1σ SD (10^{-9} cc STP g^{-1})	^{3}He/^{4}He (R_A)	^{3}He/^{4}He 1σ SD (R_A)
Columbia River Basalt							
Ilmenite							
SCAB-001	0.3393	7.34	0.18	1693.9	33.9	0.115	0.0037
SCAB-002	0.3485	7.34	0.18	2029.6	40.6	0.096	0.0031
SCAB-004	0.2930	6.89	0.18	4046.9	80.9	0.045	0.0015
SCAB-007	0.3681	12.06	0.28	1883.3	37.7	0.170	0.0052
SCAB-007-A	0.2957	12.30	0.29	1889.8	37.8	0.173	0.0053
SCAB-008	0.3244	7.94	0.20	988.3	19.8	0.214	0.0069
SCAB-017	0.2711	8.05	0.21	1832.9	36.7	0.117	0.0038
SCAB-018	0.3525	6.48	0.17	2682.1	53.6	0.064	0.0021
SCAB-025	0.3302	2.68	0.09	2505.3	50.1	0.028	0.0011
SCAB-026	0.3005	2.94	0.10	3168.1	63.4	0.025	0.0010
SCAB-030	0.2939	9.04	0.22	1936.2	38.7	0.124	0.0039
SCAB-034	0.3733	3.34	0.10	3258.4	65.2	0.027	0.0010
SCAB-039	0.3285	5.29	0.15	963.7	19.3	0.146	0.0050
SCAB-039-A	0.3089	7.04	0.18	1278.3	25.6	0.146	0.0048
SCAB-040	0.2778	5.69	0.16	2760.7	55.2	0.055	0.0019
SCAB-042	0.3034	4.51	0.13	2272.0	45.4	0.053	0.0019
Pyroxene							
SCAB-001	0.3230	9.14	0.22	538.6	10.8	0.451	0.014
SCAB-002	0.1275	8.95	0.28	151.2	3.0	1.572	0.058
SCAB-004	0.1707	8.09	0.23	396.9	7.9	0.542	0.019
SCAB-007	0.3178	15.24	0.34	185.0	3.7	2.190	0.066
SCAB-007-A	0.2253	17.45	0.40	208.2	4.2	2.227	0.068
SCAB-008	0.3064	11.41	0.27	210.8	4.2	1.438	0.045
SCAB-017	0.1947	12.63	0.32	296.6	5.9	1.132	0.037
SCAB-018	0.0400	7.43	0.45	4697.3	93.9	0.042	0.003
SCAB-025	0.3304	4.14	0.12	946.4	18.9	0.116	0.004
SCAB-026	0.3102	3.84	0.12	557.4	11.1	0.183	0.007
SCAB-030	0.3061	11.72	0.27	142.4	2.8	2.188	0.067
SCAB-034	0.0896	4.69	0.23	2380.8	47.6	0.052	0.003
SCAB-039	0.3012	7.63	0.20	637.0	12.7	0.318	0.010
SCAB-039-A	0.3094	8.21	0.20	682.6	13.7	0.320	0.010
SCAB-040	0.0819	6.86	0.30	819.2	16.4	0.222	0.011
SCAB-042	0.0349	4.55	0.42	1038.7	20.8	0.116	0.011
Snake River Plain Basalt							
Ilmenite							
P1	0.1998	4.91	0.14	533.8	10.7	0.245	0.009
P2	0.1072	6.93	0.22	190.1	3.8	0.968	0.036
P3	0.7540	3.36	0.08	37.8	0.8	2.357	0.073
P4	0.2893	5.48	0.14	399.7	8.0	0.365	0.012
P5 < 40	0.0917	3.85	0.19	68.2	1.4	1.501	0.079
P5 > 40	0.7120	4.03	0.10	84.3	1.7	1.270	0.041

at = atom; cc STP = cubic centimeters at standard temperature and pressure. Grains for samples SCAB-007-A and SCAB-039-A were crushed with a mortar and pestle prior to He measurement. He data for Snake River Plain olivine are published in Table S1 of Lamb et al. (2014).

could be separated. We measured ^{3}He in ilmenite from the Snake River Plain samples to provide an additional constraint on the production rate. Including replicate measurements for different pre-treatment and grain-size fractions, we measured He in a total of 22 paired samples of ilmenite and pyroxene or olivine.

We separated the pyroxene and ilmenite for He measurement by first crushing samples with a jaw crusher and disk mill to generate approximately 100 g of material in the 75–212 μm size fraction. The crushed rock was leached for 24 h in hot, dilute HNO_3 and then underwent a series of 3- to 5-day leaches in an HF and HNO_3 solution using an ultra-sonic bath heated to 69 °C. The initial leach was in a 1.5 L solution of 5% HF and 2% HNO_3, which was followed by a 1 L solution of 2% HF and 2% HNO_3, and, as necessary, additional leaches in 0.5 L solutions with progressively lower acid concentrations (2%, 1%, 0.5%, 0.25% HF and 2% HNO_3) until poly-mineral grains were disaggregated into single crystals. Following each leach, the acid solution was decanted and the remaining material was rinsed multiple times with water to remove fluorides. The acid leaches generally dissolved 98–99% of the initial rock

mass, resulting in single crystals of pyroxene and ilmenite, with minor plagioclase. A lithium heteropolytungstate heavy liquid was used to separate pyroxene and ilmenite from the plagioclase. Pyroxene and ilmenite grains were separated from each other with a Frantz isodynamic magnetic separator. The mineralogy of the mineral separates was confirmed via SEM EDS analysis. The same mineral separation procedure was used to separate ilmenite from the same Snake River Plain samples where He isotopic data were previously measured in olivine (Lamb et al., 2014).

Mineral grains are often crushed prior to He measurement to release mantle-sourced He from fluid inclusions and hence isolate the cosmogenic ^{3}He component (Kurz, 1986, Craig and Poreda, 1986). The small ~25–100 μm diameter pyroxene and ilmenite grains in our Columbia River Basalt samples (Fig. 1) are comparable in size to crushed grains that are typically analyzed (Amidon et al., 2009), hence we assume these fine-grained minerals contain a negligible mantle ^{3}He component. We tested this assumption with measurement of He in splits of mineral separates from two of the Columbia River Basalt samples (SCAB-007 and SCAB-039; Table 1) that were crushed under atmospheric conditions with a porcelain mortar and pestle that was first cleaned with silica-sand. Subsequently, it was proposed that adsorption of atmospheric He to mineral surfaces can contaminate grains with high specific surface areas (Protin et al., 2016). Hence, although the ilmenite from the Snake River Plain samples has similar grain sizes to the Columbia River Basalt samples, they were crushed under alcohol prior to measurement. The purpose of crushing under alcohol was to release mantle He while avoiding atmospheric ^{3}He contamination that could be introduced if the stresses imparted by crushing allows atmospheric He to enter micro-cracks that re-seal when the stresses are released. Two grain size fractions (>40 μm and <40 μm) from one Snake River Plain sample (sample P5; Table 1) were measured to assess grain size influences on He concentrations. ^{3}He and ^{4}He were measured on a MAP 215-50 noble gas spectrometer in the Caltech Noble Gas Lab following heating to 1300 °C under vacuum to release He, as described by Amidon and Farley (2011).

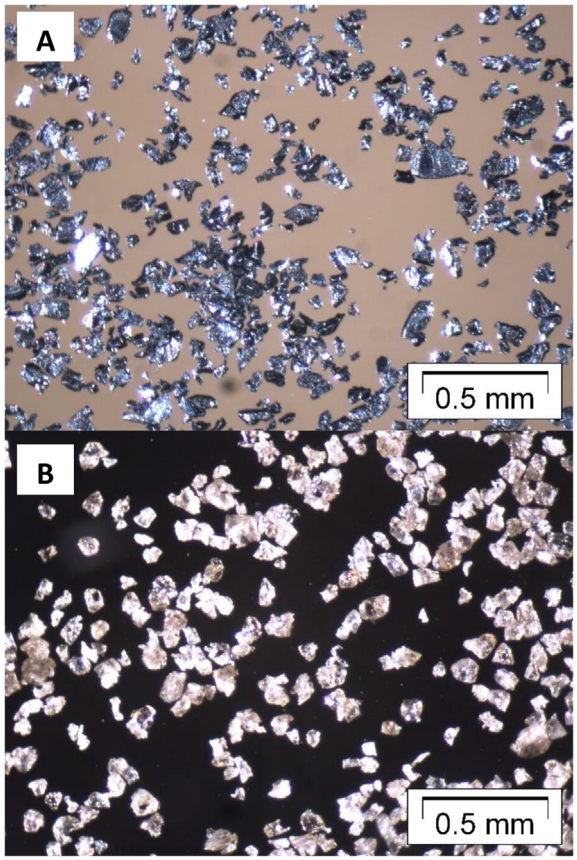

Fig. 1. Photos of mineral separates for (A) ilmenite and (B) pyroxene from sample SCAB-001.

To characterize the dimensions of ilmenite grains, we measured the dimensions of 535 ilmenite grains from SEM backscatter images taken from a thin-section of sample SCAB-017 (Fig. 2), which has ilmenite grains that are typical of the sample suite. The dimensions of pyroxene grains were not measured. Ilmenite grain size statistics were determined by measuring all grains visible in four randomly selected 2 mm by 3 mm portions of the thin section from images taken at 40× magnification (e.g., Fig. 2). The grain size statistics reported in Table 2 are calculated from the number of grains measured. The short- and long-axis dimensions were calculated from rectangular polygons manually drawn to the dimensions of each grain. The assumption of a simplified, rectangular cross-section is appropriate, as the ilmenite grains in the samples tend to have prismatic or tabular shapes. Since the orientation of individual grains relative to the plane of the thin-section is unknown, the measured dimensions only approximate the true grain dimensions. We consider them to be semi-quantitative and note that precise characterization of the crystal dimensions is not required for our first-order assessment of the role of distribution.

Whole rock chemistry and the chemistry of ilmenite and pyroxene separates was measured for the Columbia River Basalt samples. Whole rock major oxides were measured via XRF following Li-metaborate/tetraborate fusion of an aliquot of powdered rock. A suite of 58 elements, including Li, U, and Th were measured for whole rock and aliquots of ilmenite and pyroxene grains via ICP-MS following a multi-acid (HCl, HNO_3, $HClO_4$, HF) digestion. All geochemical analyses were performed by Activation Laboratories, Ontario, Canada. Chemistry was not measured for the Snake River Plain samples.

The chemistry data were used to model the production and diffusion of neutrons within rock to assess ^{3}He production by neutron capture, following Amidon et al. (2008, 2009). We predicted the number of ^{3}He atoms produced by nucleogenic and slow neutron capture reactions over 15 Ma, the age of the Wanapum Basalt (Barry et al., 2013), for a 10 μm radius spherical ilmenite crystal and pyroxene crystals of 50 and 250 μm radii.

2.2. Production rate calculation

The ratio of the ^{3}He concentration in ilmenite to that in pyroxene or olivine was determined by calculating the slope of a York regression (York, 1968) with improved estima-

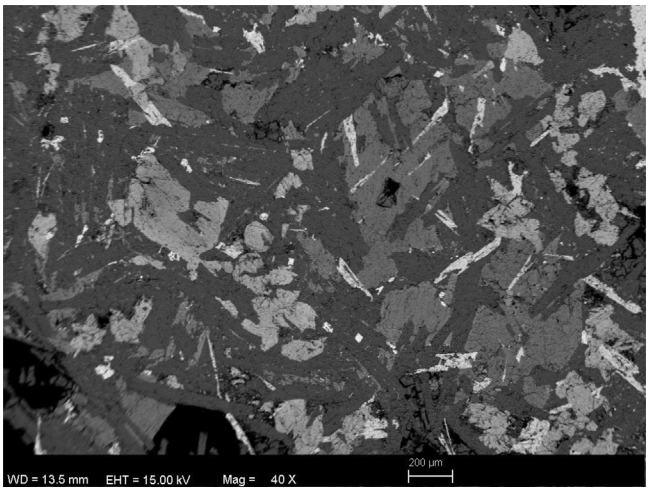

Fig. 2. SEM backscatter image of a thin section from sample SCAB-017. SEM EDS analysis indicates that lightest-colored grains with elongated or equant dimensions are ilmenite, grains with lighter grays are pyroxene, and the darker gray is plagioclase. Black areas are voids.

Table 2
Ilmenite grain size characteristics.

Statistic	Length (μm)	
	Short-axis	Long-axis
Mean	20	150
Standard deviation	18	238
Median	15	74
25th percentile	9	30
75th percentile	26	162
5th percentile	5	10
95th percentile	54	529

tion of standard errors for slope values (Mahon, 1996) with a y-intercept forced to be zero using software developed by Trappitsch et al. (2018). We calculated the uncertainty in the slope as the product of the standard error and the square root of the mean square of weighted deviates (MSWD). The resulting ratio was multiplied by the cosmogenic ^{3}He production rate in pyroxene (or, equivalently, olivine) to determine the ^{3}He production rate in ilmenite. We used a sea-level, high-latitude ^{3}He production rate of 120 $\pm$ 9.4 atom g^{-1} yr^{-1}, which is based on a compilation of previously published production rate calibration data (Goehring et al., 2010) and uses Lal-Stone scaling (Lal, 1991, Stone, 2000). The production rate value from Goehring et al. (2010) includes measurements from both olivine and pyroxene and their analysis indicates ^{3}He production rates for the two minerals agree within experimental error.

To compare our ^{3}He production rates in ilmenite with previously published values for Fe-Ti oxide minerals, we first re-calculated the published values so that all comparisons are based on the same production rates of ^{21}Ne and ^{10}Be, as these values have since been updated. Specifically, Kober et al. (2005) calibrated ^{3}He production rates in ilmenite-magnetite against the ^{21}Ne production rate in quartz, where the production rate of ^{21}Ne was constrained by the ratio of ^{21}Ne to ^{10}Be in quartz. Following Shuster et al. (2012), we used a ^{21}Ne to ^{10}Be production ratio of 4.1 $\pm$ 0.2 (Balco and Shuster, 2009) and a ^{10}Be production rate of 4.2 $\pm$ 0.2 atom g^{-1} yr^{-1} that Shuster et al. (2012) determined using data in the CRONUS calculator (Balco et al., 2008) to calculate a ^{21}Ne production rate of 17.2 $\pm$ 1.2 atom g^{-1} yr^{-1}. The ^{21}Ne production rate of 17.2 atom g^{-1} yr^{-1} is lower than the value of 20.3 atom g^{-1} yr^{-1} used by Kober et al. (2005), which results in a ^{3}He production rate of 102 $\pm$ 8 atom g^{-1} yr^{-1} that is approximately 15% lower than the originally published value.

3. RESULTS

^{3}He concentrations generally range from 3-12 million atom g^{-1} in ilmenite and 4–17 million atom g^{-1} in pyroxene (Table 1). ^{3}He/^{4}He ratios normalized to the atmospheric ratio range from 0.03-0.2 R_A for ilmenite and 0.05–2.3 R_A for pyroxene (Table 1). The ilmenite grain dimensions are small (Fig. 2); the mean length of the measured short- and long-axes are 20 μm and 150 μm, respectively (Table 2).

The measured ^{3}He ($^{3}He_{tot}$) includes multiple components (Amidon et al., 2008):

$$^{3}He_{tot} = {}^{3}He_{m} + {}^{3}He_{cn} + {}^{3}He_{nuc} + {}^{3}He_{c}$$

where $^{3}He_{m}$ is the mantle-sourced component that may be present in fluid or melt inclusions within crystals; $^{3}He_{cn}$ is the low energy cosmogenic neutron component that is produced when cosmogenically-derived low energy neutrons interact with ^{6}Li to produce ^{3}H, which decays to $^{3}He_{cn}$ (Dunai et al., 2007); $^{3}He_{nuc}$ is the nucleogenic component when α-particles generated by decay of U and Th interact with light elements via (α,*n*) reactions, and the resulting neutrons interact with ^{6}Li to produce $^{3}He_{nuc}$ (Farley et al., 2006, Amidon et al., 2008); and $^{3}He_{c}$ is the cosmogenic component produced by spallation reactions involving high energy neutrons and protons, as well as production by muons.

Here we assess the relative contributions of each component to our measured $^{3}He_{tot}$ values to isolate the $^{3}He_{c}$ com-

ponent. In this work we cannot distinguish cosmogenic production by neutrons and protons from that arising from muons. As long as the spallogenic and muonic production rate ratio is the same in the two phases, distinguishing between the two pathways is not necessary to calibrate the production rate.

Given that our mineral separation procedure generated very small ilmenite and pyroxene crystals (Fig. 1), any fluid inclusions within the crystals would be very small, as volume scales with the cube of radius, hence we assume ^3He_m does not contribute to $^3He_{tot}$ in either mineral. For the sample in which we analyzed different particle size fractions (P5), $^3He_{tot}$ of ilmenite agree for different particle sizes within uncertainty (Table 1), supporting the assumption of minimal ^3He_m. Similarly, in samples where He was measured in crushed and un-crushed grains, ^3He concentrations were either similar, or slightly higher in the crushed sample (Table 1). Among our samples the measured $^3He/^4He$ ratios vary by several orders of magnitude, likely due to substantial radiogenic ^4He production from U-Th decay over the 15 Ma since eruption of the Columbia River Basalt. We find occasional baddeleyite or zircon in our samples, which we remove via handpicking, but small grains or fragments may remain in our separates and contribute to the measured ^4He values. Due to the relatively old age of the Columbia River Basalts, it is not possible to correct for the ^3He_m component using the $^3He_m/^4He_m$ ratio established from crushing (Blard and Farley, 2008), as all ^4He cannot be assumed to originate from the mantle, hence we explicitly assume no ^3He_m. Even if the ilmenite were to have as much mantle ^3He as reported by Dodson et al. (1997), for >400 um olivine grains from a Wanapum basalt flow, it would still only account for at most 1% of what we measured.

The interaction of cosmogenic or radiogenic thermal neutrons with Li, $^6Li(n,\alpha)^3H \rightarrow ^3He$, is a potential source of $^3He_{cn}$ and $^3He_{nuc}$ (Amidon et al., 2008). The results of our nucleogenic and slow neutron capture modeling show that for the 1–6 ppm range of Li concentrations in our ilmenite grains (Table S1), the $^3He_{cn}$ and $^3He_{nuc}$ components are predicted to be 0.05–0.07 and 0.24–0.33 million atoms g^{-1}, respectively (Fig. 3a), after 15 Ma of ingrowth. Similarly, model results for a range of pyroxene grain sizes suggest the sum of the $^3He_{cn}$ and $^3He_{nuc}$ components are similar, on the order of 0.4–0.6 million atom g^{-1} (Fig. 3b). Hence the sum of the $^3He_{cn}$ and $^3He_{nuc}$ components in ilmenite and pyroxene are at maximum ~10% of $^3He_{tot}$. Importantly, the total number of predicted $^3He_{cn}$ and $^3He_{nuc}$ atoms are comparable for ilmenite and pyroxene crystals, suggesting these components do not substantially influence the $^3He_{tot}$ ratios between the two minerals. Because $^3He_{cn}$ and $^3He_{nuc}$ accumulate linearly with time, their contribution to $^3He_{tot}$ in the much younger Snake River Plain samples would be an order of magnitude lower than for the Columbia River Basalt samples.

The expected minimal contribution of ^3He_m, $^3He_{cn}$ and $^3He_{nuc}$ allow us to assume that $^3He_c = {}^3He_{tot}$. Therefore, the ratio of the concentration of ^3He in ilmenite to that in pyroxene or olivine, which is 0.78 ± 0.02 (Fig. 4), should equal the ^3He_c production ratio between the two minerals.

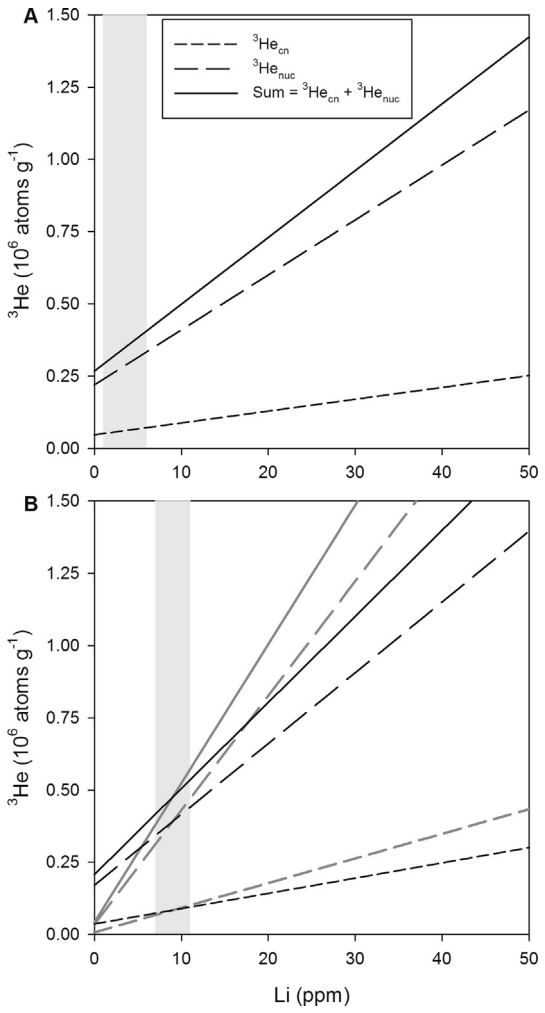

Fig. 3. Modeled $^3He_{cn}$ and $^3He_{nuc}$ production over 15 Ma. (A) Results for a 10 μm radius grain which is the half thickness of the mean of measured short-axis values for ilmenite (Table 2); (B) results for a 50 μm (black) and 250 μm radius (gray) grains which span the range of pyroxene grains in our samples. Gray bar shows range of measured Li concentrations in each mineral phase (Table S1).

Based on the calibrated production rate in pyroxene and olivine (Goehring et al., 2010), we find that the ^3He_c apparent production rate in ilmenite is 93.6 ± 7.7 atoms g^{-1} yr^{-1}. This ^3He production rate is about 30% greater than the theoretical prediction of 67 atoms g^{-1} yr^{-1} (Masarik and Reedy, 1996) and the rate obtained by Shuster et al. (2012) on hematite. It is also higher than the estimated rate of Margerison et al. (2005) of 72–78 atoms g^{-1} yr^{-1}. However, the re-scaled production rates in magnetite-ilmenite from Kober et al. (2005) are 102 ± 8 atoms g^{-1} yr^{-1}, which is within uncertainty of our predicted values. Thus, with the exception of the Kober et al. (2005) dataset, the ^3He_c production rate we predict is notably higher than expected based on previous production rate work.

Substitution of atoms with contrasting production rates could cause production rates to differ, as ^3He_c production rates from Mg are three times higher than from Fe

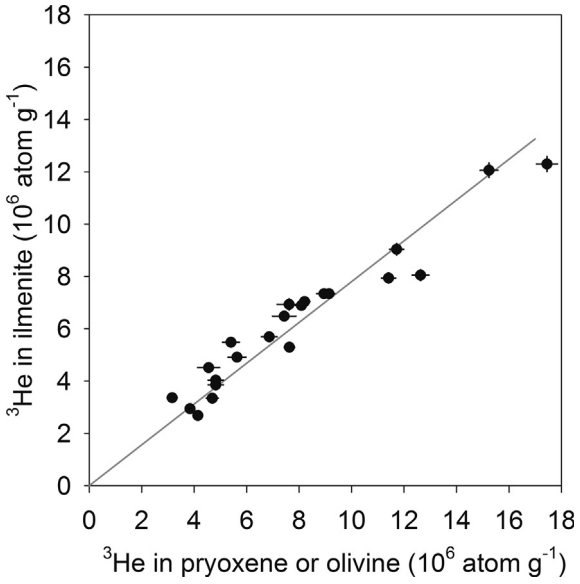

Fig. 4. The concentration of ^{3}He in ilmenite versus ^{3}He in pyroxene or olivine. The slope is 0.78 ± 0.02 where the uncertainty is calculated as the product of one standard error (0.0072) in the slope estimate and the square root of the MSWD (7.87). The error bars denote the 1 sigma SD for the ^{3}He measurements; those that are not visible are smaller than the symbols.

(Masarik and Reedy, 1996) and Mg concentrations in Fe-Ti oxide minerals are variable (Darby 1984, Basu and Molinaroli, 1989, Lee et al., 2005, McEnroe et al., 2007). However, our ilmenite grains contain $< 1\%$ Mg (Table S1), so substitution of Mg for Fe cannot explain the apparently higher production rate. In the next section we model the redistribution of spallation ^{3}He in order to reconcile our measured rates, previous measurements, and theory.

4. ANALYSIS: REDISTRIBUTION OF SPALLATION ^{3}HE

Most prior ^{3}He$_c$ production rate calibration work has used coarse-grained olivine or pyroxene crystals, which have compositions that are generally similar to the basalt they are hosted in. Our study differs in this regard, in that the ilmenite phase is both very fine-grained and of a composition very distinct from the basalt host. Under these circumstances redistribution of the spallation products between adjacent minerals is potentially important, yet the influence of redistribution on ^{3}He$_c$ concentrations in different mineral phases has not previously been considered. In this section we assess whether redistribution could account for the high ^{3}He production rate we obtained. Our goal is to approximate the influence of redistribution to first-order, and thus we have made some simplifying assumptions, such as spherical, rather than tabular or blade-like ilmenite crystals and that the whole rock chemistry approximates that of grains adjacent to ilmenite. The approximations allow for a semi-quantitative assessment of the roles that grain-size and redistribution play in determining apparent ^{3}He$_c$ production rates in ilmenite.

Cosmogenic ^{3}He is primarily produced when high energy cosmic rays induce nuclear spallation of target nuclei. Spallation is a very energetic process, with much of the energy carried off as motion, typically by many micrometers, of the spalled ^{3}He nucleus. Ejection of spallation products from small micrometeorites and pre-solar grains in space has been predicted and modeled (Pepin et al., 2001). Similar effects must exist for spallation occurring in minerals within rocks exposed to secondary cosmic rays (mostly neutrons) on the Earth's surface, with the additional complexity that both ejection and injection can occur. Thus in a rock-hosted mineral grain, the cosmogenic ^{3}He production rate in the grain is sensitive not only to the production rate within the grain, but also to the production rate in its surroundings (Farley et al., 2006). In addition, variations in mass stopping power among constituent grains of a rock will influence where spalled ^{3}He and ^{3}H are stopped. We here use the term redistribution to refer to the consequences of long stopping ranges on the ultimate location of spalled ^{3}He (both directly produced and via ^{3}H). The question to be addressed is the quantitative consequences of redistribution, and under what conditions of grain size and chemistry is redistribution important.

The energy spectra of ^{3}He-producing spallation reactions in terrestrial rock was recently modeled by Nesterenok and Yakubovich (2016). Their model assumes an average upper continental crust composition and sea level cosmic ray exposure. We adopt their results for our modeling, recognizing that small differences likely exist under other chemistry and elevation scenarios.

Fig. 5 shows the Nesterenok and Yakubovich (2016) energy spectra of ^{3}H and ^{3}He spallation along with the

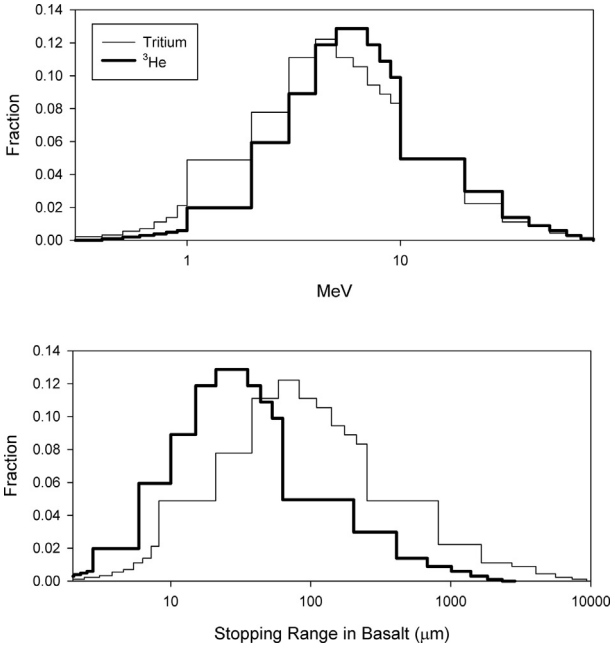

Fig. 5. Upper panel: Energy spectra of spallation ^{3}H and ^{3}He from Nesterenok and Yakubovich (2016). Lower Panel: stopping ranges for energy distributions in upper panel computed using SRIM (Ziegler et al., 2010) and assuming whole rock basalt chemistry and density.

stopping distance of these particles in a rock of typical Columbia River Basalt chemistry (Hooper, 2000; see caption to Table 3) and density 2.9 g/cm^3, computed using SRIM (Ziegler et al., 2010). Stopping distances range from <1 μm to as long as a few mm, with a peak in the ^{3}He distribution at about 30 μm and in the ^{3}H distribution at 70 μm. Intuitively, redistribution effects become important when grain sizes are similar to or smaller than these stopping distances. Because grains analyzed for ^3He_c, e.g., olivine in basalt, are typically within this size range, and our ilmenites are certainly in this range, redistribution effects are potentially important.

4.1. General effects of redistribution

In this section we establish the maximum effect possible from redistribution of spallation ^{3}He. Consider a small chemically-distinct mineral grain (call it ***g***) in an otherwise homogenous host rock. The apparent production rate of ^3He_c in the grain (P_g) includes ^{3}He produced in and retained in that grain (P_{ret}) and ^{3}He produced in the host rock but injected into the grain (P_{inj}).

$$P_g = P_{inj} + P_{ret} \quad (1)$$

Here the term apparent production rate is used to distinguish the true production rate (P_G) in a grain of a size large (hence the capital G subscript) compared to spallation stopping distances from the apparent production rate (P_g) that applies to a small grain of the same composition in which redistribution effects are important. The goal of this section is to describe mathematically how P_g, the apparent production rate in ***g***, relates to the independently known production rate in the host (P_H) and the true production rate in ***G*** (P_G). P_G differs from P_H because the two phases differ in chemical composition. An additional complication considered in the next section is that ^{3}He is produced both by direct spallation to ^{3}He and via spallation of ^{3}H followed by rapid decay to ^{3}He.

Defining fractional redistribution coefficients as follows:

$$F_{inj} = (\text{atoms/g injected into } \boldsymbol{g})/(\text{atoms/g produced in host})$$

$$F_{ret} = (\text{atoms/g retained in } \boldsymbol{g})/(\text{atoms/g produced in } \boldsymbol{g})$$

and combining with Eq. (1) yields:

$$P_g = F_{inj}P_H + F_{ret}P_G \quad (2)$$

A useful way to represent the consequences of spallation ^{3}He redistribution is to ratio the apparent production rate (P_g) to the true production rate (P_G):

$$P_g/P_G = F_{inj}(P_H/P_G) + F_{ret} \quad (3)$$

Previous workers presented approximations for assessing the effects of redistribution of energetic He ions among phases (Farley et al., 1996, Dunai et al., 2007), but these approximations are not accurate in the case of grains that are close to or smaller than the stopping distance of the emitted particle, as is the case here. Nor do these models consider the effects of differential mass stopping power between the host and grain of interest.

As demonstrated in the next section, the grain size below which spallation ^{3}He redistribution effects become significant is 0.5 mm in diameter. Before considering how the effect varies with grain size, it is useful to consider the maximum possible effect and to identify its controls. In the limit of a grain size so small that ^{3}He is completely ejected from ***g***, all ^{3}He within ***g*** comes from spallation in the host and subsequent injection. If ***g*** is an isolated grain in an otherwise homogenous host, then the overall production rate in the system is well-approximated by that of the host, and the relative abundance of spalled particles ultimately residing in each phase is dictated by the relative stopping power of the phases (S_g and S_H respectively, in MeV mg^{-1} cm^{-2}). In this limit $F_{ret} = 0$, $F_{inj} = S\boldsymbol{g}/S_H$, and Eq. (3) becomes:

$$P\boldsymbol{g}/P_G = (S\boldsymbol{g}/S_H)(P_H/P_G) \quad (4)$$

Stopping power of a medium increases with the medium's density and decreases with its mean atomic number (Ziegler et al., 2010). By expressing F_{inj} on a per gram basis, the effect of variations in density between ***g*** and host on stopping power are eliminated. For example, if ***g*** is twice as dense as the host but has the same stopping power in

Table 3
Mass stopping powers and cosmogenic ^{3}He production rates.

Material	MSP Mev/mg/cm^2	MSP Normalized	^{3}He PR Atoms/g/yr	^{3}He PR Normalized	P_g/P_G
basalt	**0.437**	**1**	**110**	**1**	**1**
water	0.594	1.36	120	1.091	1.24
air	0.492	1.12	152	1.382	0.81
quartz	0.450	1.03	124	1.127	0.91
enstatite	0.448	1.03	123	1.118	0.92
forsterite	0.447	1.02	123	1.118	0.91
fluroapatite	0.431	0.99	98	0.891	1.11
ilmenite	0.377	0.86	77	0.700	1.23
hematite	0.370	0.85	69	0.627	1.35
pyrite	0.364	0.83	64	0.582	1.43
zircon	0.359	0.82	64	0.582	1.41

Assumes stoichiometric endmember mineral chemistry. MSP: mass stopping power at 7 Mev for ^{3}He (Ziegler et al., 2010); normalized: ratioed to basalt; PR: cosmogenic ^{3}He production rate based on chemistry and element-specific production rates (Masarik and Reedy, 1996); P_g/P_G: see Eq. (4); assumed basalt chemistry for the Columbia River Basalt (Hooper, 2000): SiO_2 51.3%; TiO_2 2.68%, Al_2O_3 13.94%; FeO 12.84%; MgO 5.43%; CaO 9.1%, Na_2O 2.89%; K_2O 1.05%.

MeV/μm, there will be a factor of two higher probability of a particle stopping in a unit volume of ***g*** compared to the host. This difference is exactly compensated by that volume's two-fold greater mass. In contrast, variations in mean atomic number and resulting differences in density-normalized stopping power are not eliminated.

Table 3 lists the mass stopping power of several mineral phases to quantitatively illustrate the effects of differential stopping power. For comparison, all are normalized to the mass stopping power of a basalt of typical composition and are computed for a 7 MeV ^{3}He ion. Common mineral phases made up of mostly light elements (e.g., quartz, forsterite, enstatite) have mass stopping powers that differ from that of basalt by just a few percent. In contrast, minerals with higher mean atomic number such as ilmenite, hematite, zircon, and pyrite have substantially lower mass stopping powers. There is no noticeable difference between ^{3}He and ^{3}H mass stopping powers normalized in this fashion. Nor would there be significant differences if the relative stopping powers were computed at a higher or lower energy.

Eq. (4) has two terms, relative mass stopping power ($S\boldsymbol{g}/S_H$) and the reciprocal of the relative spallation ^{3}He production rates (P_H/P_G). Like mass stopping power, spallation production rate (in atoms mass^{-1} time^{-1}) also decreases with mean atomic number (Z), and as a result the two terms are roughly anti-correlated. This is illustrated in Table 3 using element specific production rates (Masarik and Reedy, 1996). The results show that in this small grain limit (Eq. (4)), the maximum deviation for commonly ^{3}He-dated phases like olivine and pyroxene in basalt is about −9%, i.e., the apparent production rate in a very small grain will be about 9% lower than in grains larger than ~500 μm diameter. The explanation for this observation is that the production rate of ^{3}He in the host basalt (and implanted in the tiny olivine) is ~11% lower than the production rate in pure coarse olivine, but this is partially compensated for by the fact that olivine and pyroxene have mass stopping powers about 2% higher than basalt. Stated differently, the mass stopping power term decreases with Z more slowly than does the spallation production rate term, so the two terms in Eq. (4) don't completely compensate.

The consequences for phases with mean atomic number much higher than the host are more noticeable. For example, Table 3 shows that the maximum effect is +23% for ilmenite in basalt and +43% for pyrite in basalt. While a ~10% effect is potentially undetectable given a host of other uncertainties in production rate estimates, effects >20% are large enough that they need to be considered when assigning exposure ages or erosion rates based on cosmogenic ^{3}He data.

4.2. Variation with grain size

We used a Monte Carlo simulation similar to that developed for calculation of the α ejection correction factor in (U-Th)/He dating (Farley et al., 1996) to assess spallation ^{3}He redistribution. The model setup consists of an isolated sphere of radius R centered in a uniform host of a different chemical composition and density. The Monte Carlo model simulates the slowing down of a spalled ^{3}He or ^{3}H nucleus from a random location and along a randomly selected trajectory through the system. Slowing is governed by the energy and material-specific stopping powers computed with SRIM (Ziegler et al., 2010). The trajectory is assumed to be linear. After simulation of many millions of spallation events, the concentration of particles coming to rest in the central grain due to implantation and due to retention are computed and normalized to the production rate to yield F_{inj} and F_{ret}.

As found for α particle ejection (Farley et al., 1996), the key variable governing spallation ^{3}He redistribution is the ratio of the stopping distance to the size of the grain of interest, S/R. Fig. 6 shows F_{inj} and F_{ret} results computed from the Monte Carlo simulation consisting of a model ilmenite grain in a basaltic host. The fraction of ions retained (F_{ret}) starts at unity for S/R near zero and declines to zero at S/R = 2; at this value of S/R the stopping distance is longer than the longest possible path through the grain so no spalled nuclei can remain in the central grain. Similarly, for implantation, F_{inj} starts at zero and rises steadily until S/R = 2 as spalled particles penetrate more and more deeply into the central grain. Above S/R = 2, F_{inj} achieves the mass stopping power limit described in the previous section (which is 0.86 for ilmenite in basalt; Table 3).

Fig. 7 takes the results shown in Fig. 6 and weights the stopping distances for the energy spectra shown in Fig. 5 and assumes a value of unity for the spallation production pathway ratio of ^{3}He/^{3}H. This figure shows F_{inj} and F_{ret} integrated across the entire energy distribution and nuclide pathway as a function of grain size. It was specifically computed for the ilmenite-in-basalt example. Fig. 7 allows the final step of the computation, weighting the injected and retained fractions by the spallation production rate in the host and ***g***, respectively (Eq. (3)). Fig. 8 shows the result in the case of ilmenite and basalt using the relative spallation production rates shown in Table 3. As indicated from

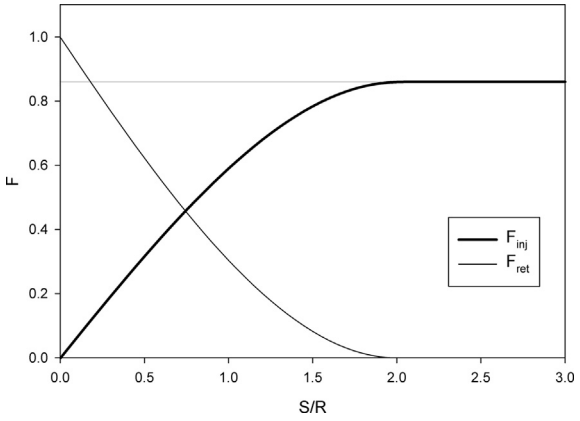

Fig. 6. Results of Monte Carlo simulation for the injected and retained fractions as a function of the ratio of the stopping distance of an energetic ^{3}He or ^{3}H ion in the central grain divided by that grain's radius. This example was computed for ilmenite in a basalt of the composition given in the caption to Table 3. F_{inj} ultimately reaches the stopping power ratio for these two phases, 0.86 (horizontal line; see Table 3).

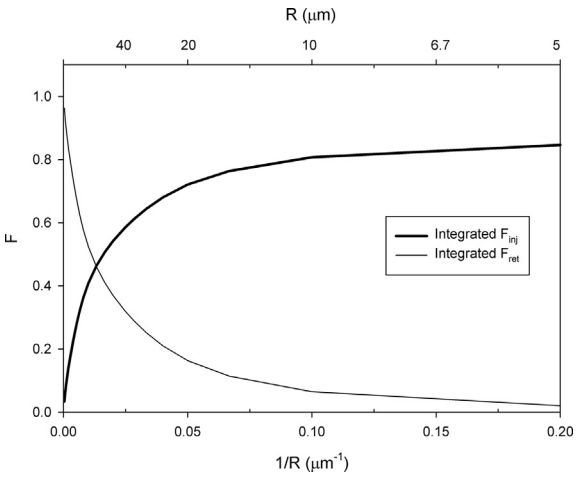

Fig. 7. Injection and retention curves for the ilmenite-in-basalt example integrated across the entire spallation energy distribution and ^{3}H and ^{3}He pathways. R is the radius of the central grain.

the small grain limit estimate, P_g the apparent production rate is about 23% higher in very fine-grained (few micron) ilmenite hosted in basalt compared with a specimen of ilmenite free of redistribution effects. By 50 μm radius the effect has fallen to ~+15% and by 250 μm to ~+5%. Ilmenite grains in basalt are typically not equant (sphere-like), but are often tabular- or blade-shaped. For such geometries the half-thickness of the smallest dimension is a reasonable approximation to the spherical radius used in modeling, at least for semi-quantitative application.

Following the same procedure, we also calculated the effects of spallation redistribution for olivine in basalt. As shown in Fig. 8, the effect ranges from ~−9% at a few micron grain size, rises to −6% at 50 μm radius, and by 500 μm reaches ~−1%.

5. DISCUSSION

The ilmenite grain dimensions in our samples vary but generally range from a few to a few tens of microns in cross section. Using the mean cross section of 20 μm (R = 10 μm, the half-thickness of a tabular- or blade-shaped grain) the results shown in Fig. 8 semi-quantitatively predict an apparent production rate 22% higher than the true production rate. Starting with our empirically-determined production rate of 93.6 ± 7.7 atoms g^{-1} yr^{-1} and reducing it by 22% to subtract the implanted component of ^{3}He$_c$ yields a production rate of 73.0 ± 6.0 atoms g^{-1} yr^{-1}. Hence accounting for net implantation in our small ilmenite grains results in a production rate estimate that agrees within error with the hematite production rate of 68.1 ± 8.1 atoms g^{-1} yr^{-1} (Shuster et al., 2012) and is comparable to the 72–78 atoms g^{-1} yr^{-1} ilmenite production rate of Margerison et al. (2005). The Shuster et al. (2012) measurements were made on massive hematite and the Margerison et al. (2005) measurements were made on the 125–250 μm fraction of crushed grains, both of which are grain sizes where we predict redistribution of ^{3}He and ^{3}H to be negligible. Hence our analysis suggests that redistribution of spallation ^{3}He and ^{3}H is a reasonable explanation for the higher apparent production rates we observe. The mean diameter of ilmenite-magnetite grains measured by Kober et al. (2005) was 0.3 mm and separates included grains up to 1 mm in diameter, hence redistribution likely does not account for the higher production rate of 102 ± 8 atoms g^{-1} yr^{-1} determined by their study, nor could they explain why their production rate estimates were higher than previous estimates (Kober, et al., 2005).

Our analysis of ^{3}He redistribution shows that the production rate in ilmenite and the host rock and the size of the ilmenite grains all influence the apparent production rate. The ^{3}He production rate in ilmenite and basalt are unlikely to vary considerably among natural specimens. Hence except in cases where there are substitutions for Fe in ilmenite or where ilmenite is hosted in a different type of rock, such as granite, the grain size of the ilmenite primarily controls the apparent production rate. If the sizes of ilmenite grains in the Columbia River and Snake River Plain basalts are typical, then our results can be generalized to other basalt provinces. However, given the importance of grain size in influencing ^{3}He$_c$ production rates, if grain sizes are unknown, they should be characterized. Accounting for

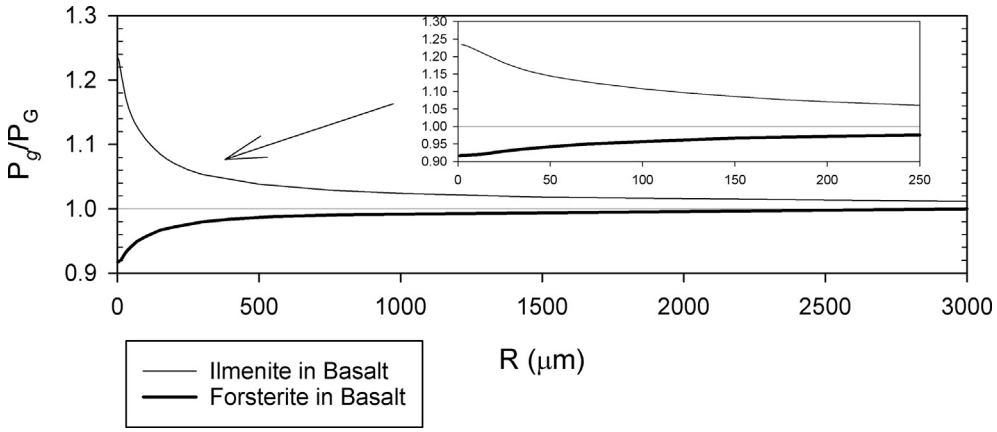

Fig. 8. Consequences of spallation ^{3}He and ^{3}H redistribution on the apparent production rate of ilmenite in basalt and forsterite in basalt as a function of the target mineral grain radius in the rock.

grain-size has the potential to avoid systematic overprediction of exposure ages or underprediction of erosion rates, which we have demonstrated can exceed 20% if the lower production rate of Margerison et al. (2005) is assumed for small ilmenite crystals. The volume fraction of ilmenite relative to groundmass and the spatial distribution of ilmenite – whether it is uniformly distributed or clustered – will likely have additional but relatively small influences on the apparent production rate. A more important factor is likely the skewness of the ilmenite grain size distribution, as in an aliquot of grains, the larger grains will contribute relatively more ^{3}He to the measurement than smaller grains. Given the difficulty in accurately characterizing crystal dimensions, at small grain sizes there will inevitably be uncertainty of at least several percent in the apparent ^3He_c production rate in ilmenite.

6. CONCLUSIONS

We measured ^{3}He in ilmenite and pyroxene or olivine from samples of Columbia River and Snake River Plain basalt. The ^{3}He is primarily cosmogenic in origin, hence we calculate the apparent cosmogenic ^{3}He production rate ratio in ilmenite to pyroxene (or equivalently, olivine) to be 0.78 ± 0.02. Based on prior production rate calibration work on pyroxene and olivine, the apparent cosmogenic ^{3}He production rate in ilmenite in our samples is 93.6 $\pm$ 7.7 atom g^{-1} yr^{-1}. Our apparent production rate is 20–30% greater than expected from prior estimates on compositionally similar minerals. Unlike previous studies, we measured ^{3}He in small ~20 μm cross-section ilmenite grains. ^{3}He and ^{3}H produced by high energy spallation reactions have long-stopping distances relative to small grains, leading to net implantation of ^{3}He in ilmenite from the surrounding rock. The anomalously high production rate is caused by net implantation of spallation products from the host rock, where production rates are high relative to ilmenite. Redistribution modeling indicates that for the small dimension of the ilmenite grains in our samples, redistribution of ^{3}He and ^{3}H leads to apparent production rates that are ~22% greater than those in large grains, which resolves within uncertainty the discrepancy between our calibrated production rate, theory and most rates from previous work. The apparent ^{3}He production rate depends on the production rate in ilmenite and the whole rock, and the grain size of the ilmenite. Whereas ilmenite and whole rock production rates are not expected to vary considerably among basalts, the ilmenite grain size may vary, indicating grain size should be quantified to reduce uncertainly in exposure ages and erosion rates determined by measuring ^{3}He in ilmenite.

ACKNOWLEDGEMENTS

We thank George Rossman, Chi Ma, and Michael Jercinovic for assistance with mineral characterization and Lindsey Hedges, Ryan McKeon, Elliot Simon, and Derek Berman for laboratory assistance. We thank Ben Mackey for making his SRP samples and his analyses of He in olivine available and Willy Amidon for sharing and providing guidance in using his code to model ^{3}He production via neutron capture. We thank Pieter Vermeesch and two anonymous reviewers for constructive comments.

FUNDING SOURCES

This research was supported by a collaborative NSF award (1529528, 1529110) to I.J.L. K.A.F., and M.P.L. and NASA grant NNX13AM83G to MPL.

APPENDIX A. SUPPLEMENTARY DATA

Supplementary data to this article can be found online at https://doi.org/10.1016/j.gca.2019.08.025.

REFERENCES

Ackert, Jr, R. P., Singer B. S., Guillou H., Kaplan M. R. and Kurz M. D. (2003) Long-term cosmogenic ^{3}He production rates from ^{40}Ar/^{39}Ar and K-Ar dated Patagonian lava flows at 47°S. *Earth Planet. Sci. Lett.* **210**, 119–136.

Amidon W. H. and Farley K. A. (2012) Cosmogenic ^{3}He and ^{21}Ne dating of biotite and hornblende. *Earth Planet. Sci. Lett.* **313**, 86–94.

Amidon W. H. and Farley K. A. (2011) Cosmogenic ^{3}He production rates in apatite, zircon and pyroxene inferred from Bonneville flood erosional surfaces. *Quat. Geochronol.* **6**, 10–21.

Amidon W. H., Farley K. A., Burbank D. W. and Pratt-Sitaula B. (2008) Anomalous cosmogenic ^{3}He production and elevation scaling in the high Himalaya. *Earth Planet. Sci. Lett.* **265**, 287–301.

Amidon W. H., Rood D. H. and Farley K. A. (2009) Cosmogenic ^{3}He and ^{21}Ne production rates calibrated against ^{10}Be in minerals from the Coso volcanic field. *Earth Planet. Sci. Lett.* **280**, 194–204.

Balco G., Stone J. O., Lifton N. A. and Dunai T. J. (2008) A complete and easily accessible means of calculating surface exposure ages or erosion rates from ^{10}Be and ^{26}Al measurements. *Quat. Geochronol.* **3**, 174–195.

Balco G. and Shuster D. L. (2009) Production rate of cosmogenic ^{21}Ne in quartz estimated from ^{10}Be, ^{26}Al, and ^{21}Ne concentrations in slowly eroding Antarctic bedrock surfaces. *Earth Planet. Sci. Lett.* **281**, 48–58.

Barry T., Kelley S., Reidel S., Camp V., Self S., Jarboe N., Duncan R., Renne P., Ross M. and Wolff J. (2013) Eruption chronology of the Columbia River Basalt Group. *The Columbia River Flood Basalt Province: Geological Society of America Special Paper* **497**, 45–66.

Basu A. and Molinaroli E. (1989) Provenance characteristics of detrital opaque Fe-Ti oxide minerals. *J. Sediment. Res.* **59**, 922–934.

Baynes E. R., Attal M., Niedermann S., Kirstein L. A., Dugmore A. J. and Naylor M. (2015) Erosion during extreme flood events dominates Holocene canyon evolution in northeast Iceland. *Proc. Natl. Acad. Sci. USA* **112**, 2355–2360.

Blard P., Lavé J., Sylvestre F., Placzek C., Claude C., Galy V., Condom T. and Tibari B. (2013) Cosmogenic ^{3}He production rate in the high tropical Andes (3800 m, 20°S): implications for the local last glacial maximum. *Earth Planet. Sci. Lett.* **377**, 260–275.

Blard P., Lavé J., Pik R., Wagnon P. and Bourlès D. (2007) Persistence of full glacial conditions in the central Pacific until 15,000 years ago. *Nature* **449**, 591.

Blard P. and Farley K. (2008) The influence of radiogenic ^{4}He on cosmogenic ^{3}He determinations in volcanic olivine and pyroxene. *Earth Planet. Sci. Lett.* **276**, 20–29.

Bretz J. H. (1923) The channeled scablands of the Columbia Plateau. *J. Geol.* **31**, 617–649.

Bromley G. R., Hall B. L., Schaefer J. M., Winckler G., Todd C. E. and Rademaker K. M. (2011) Glacier fluctuations in the southern Peruvian Andes during the late-glacial period, constrained with cosmogenic ^{3}He. *J. Quat. Sci.* **26**, 37–43.

Cerling T. E. (1990) Dating geomorphologic surfaces using cosmogenic ^{3}He. *Quatern. Res.* **33**, 148–156.

Cerling T. E. and Craig H. S. (1994a) Geomorphology and in-situ cosmogenic isotopes. *Annu. Rev. Earth Planet. Sci.* **22**, 273–317.

Cerling T. E., Webb R. H., Poreda R. J., Rigby A. D. and Melis T. S. (1999) Cosmogenic ^{3}He ages and frequency of late Holocene debris flows from Prospect Canyon, Grand Canyon, USA. *Geomorphology* **27**, 93–111.

Cerling T. E. and Craig H. (1994b) Cosmogenic ^{3}He production rates from 39°N to 46°N latitude, western USA and France. *Geochim. Cosmochim. Acta* **58**, 249–255.

Cerling T. E., Poreda R. J. and Rathburn S. L. (1994) Cosmogenic ^{3}He and ^{21}Ne age of the Big Lost River flood, Snake River Plain, Idaho. *Geology* **22**, 227–230.

Craig H. and Poreda R. J. (1986) Cosmogenic He in terrestrial rocks: The summit lavas of Maui. *Proc. Natl. Acad. Sci. USA* **83**, 1970–1974.

Darby D. A. (1984) Trace elements in ilmenite: a way to discriminate provenance or age in coastal sands. *Geol. Soc. Am. Bull.* **95**, 1208–1218.

Dodson A., Kennedy B. M. and DePaolo D. J. (1997) Helium and neon isotopes in the Imnaha Basalt, Columbia River Basalt Group: evidence for a Yellowstone plume source. *Earth Planet. Sci. Lett.* **150**, 443–451.

Dunai T. J., Stuart F. M., Pik R., Burnard P. and Gayer E. (2007) Production of ^{3}He in crustal rocks by cosmogenic thermal neutrons. *Earth Planet. Sci. Lett.* **258**, 228–236.

Dunai T. J. and Wijbrans J. R. (2000) Long-term cosmogenic ^{3}He production rates (152 ka–1.35 Ma) from ^{40}Ar/^{39}Ar dated basalt flows at 29°N latitude. *Earth Planet. Sci. Lett.* **176**, 147–156.

Farley K. (2018) Helium diffusion parameters of hematite from a single-diffusion-domain crystal. *Geochim. Cosmochim. Acta* **231**, 117–129.

Farley K., Wolf R. and Silver L. (1996) The effects of long alpha-stopping distances on (U-Th)/He ages. *Geochim. Cosmochim. Acta* **60**, 4223–4229.

Farley K., Libarkin J., Mukhopadhyay S. and Amidon W. (2006) Cosmogenic and nucleogenic ^{3}He in apatite, titanite, and zircon. *Earth Planet. Sci. Lett.* **248**, 451–461.

Fenton C. R. and Niedermann S. (2014) Surface exposure dating of young basalts (1–200 ka) in the San Francisco volcanic field (Arizona, USA) using cosmogenic ^{3}He and ^{21}Ne. *Quat. Geochronol.* **19**, 87–105.

Ferrier K. L., Perron J. T., Mukhopadhyay S., Rosener M., Stock J. D., Huppert K. L. and Slosberg M. (2013) Covariation of climate and long-term erosion rates across a steep rainfall gradient on the Hawaiian island of Kaua'i. *Geol. Soc. Am. Bull.* **125**, 1146–1163.

Force E. R. (1991) Geology of titanium-mineral deposits. *Geol. Soc. Am. Spec. Pap.* **259**.

Gayer E., Pik R., Lavé J., France-Lanord C., Bourles D. and Marty B. (2004) Cosmogenic ^{3}He in Himalayan garnets indicating an altitude dependence of the ^{3}He/^{10}Be production ratio. *Earth Planet. Sci. Lett.* **229**, 91–104.

Gayer E., Mukhopadhyay S. and Meade B. J. (2008) Spatial variability of erosion rates inferred from the frequency distribution of cosmogenic ^{3}He in olivines from Hawaiian river sediments. *Earth Planet. Sci. Lett.* **266**, 303–315.

Goehring B. M., Kurz M. D., Balco G., Schaefer J. M., Licciardi J. and Lifton N. (2010) A reevaluation of in situ cosmogenic ^{3}He production rates. *Quat. Geochronol.* **5**, 410–418.

Goldich S. S. (1938) A study in rock-weathering. *J. Geol.*, 17–58.

Hart S. (1984) He diffusion in olivine. *Earth Planet. Sci. Lett.* **70**, 297–302.

Hooper P. R. (2000) Chemical discrimination of Columbia River basalt flows. *Geochem. Geophys. Geosyst.* **1**, 1024. https://doi.org/10.1029/2000GC000040.

Kober F., Ivy-Ochs S., Leya I., Baur H., Magna T., Wieler R. and Kubik P. (2005) In situ cosmogenic ^{10}Be and ^{21}Ne in sanidine and in situ cosmogenic ^{3}He in Fe–Ti-oxide minerals. *Earth Planet. Sci. Lett.* **236**, 404–418.

Kurz M. D. (1986) In situ production of terrestrial cosmogenic helium and some applications to geochronology. *Geochim. Cosmochim. Acta* **50**, 2855–2862.

Kurz M. D., Colodner D., Trull T. W., Moore R. B. and O'Brien K. (1990) Cosmic ray exposure dating with in situ produced cosmogenic ^{3}He: results from young Hawaiian lava flows. *Earth Planet. Sci. Lett.* **97**, 177–189.

Lal D. (1991) Cosmic ray labeling of erosion surfaces: in situ nuclide production rates and erosion models. *Earth Planet. Sci. Lett.* **104**, 424–439.

Lamb M. P., Mackey B. H. and Farley K. A. (2014) Amphitheater-headed canyons formed by megaflooding at Malad Gorge, Idaho. *Proc. Natl. Acad. Sci. USA* **111**, 57–62.

Laughlin A. W., Poths J., Healey H. A., Reneau S. and WoldeGabriel G. (1994) Dating of Quaternary basalts using the cosmogenic ^{3}He and ^{14}C methods with implications for excess ^{40}Ar. *Geology* **22**, 135–138.

Lee M. J., Lee J. I. and Moutte J. (2005) Compositional variation of Fe–Ti oxides from the Sokli complex, northeastern Finland. *Geosci. J.* **9**, 1–13.

Licciardi J., Kurz M., Clark P. and Brook E. (1999) Calibration of cosmogenic ^{3}He production rates from Holocene lava flows in Oregon, USA, and effects of the Earth's magnetic field. *Earth Planet. Sci. Lett.* **172**, 261–271.

Licciardi J. M., Clark P. U., Brook E. J., Pierce K. L., Kurz M. D., Elmore D. and Sharma P. (2001) Cosmogenic ^{3}He and ^{10}Be chronologies of the late Pinedale northern Yellowstone ice cap, Montana, USA. *Geology* **29**, 1095–1098.

Mackey B. H. and Quigley M. C. (2014) Strong proximal earthquakes revealed by cosmogenic ^{3}He dating of prehistoric rockfalls, Christchurch, New Zealand. *Geology* **42**, 975–978.

Mackey B. H., Scheingross J. S., Lamb M. P. and Farley K. A. (2014) Knickpoint formation, rapid propagation, and landscape response following coastal cliff retreat at the last interglacial sea-level highstand: Kaua'i, Hawai'i. *Geol. Soc. Am. Bull.* **126**, 925–942.

Mahon K. I. (1996) The new "York" regression: application of an improved statistical method to geochemistry. *Int. Geol. Rev.* **38**, 293–303.

Marchetti D. W. and Cerling T. E. (2005) Cosmogenic ^{3}He exposure ages of Pleistocene debris flows and desert pavements in Capitol Reef National Park, Utah. *Geomorphology* **67**, 423–435.

Margerison H., Phillips W., Stuart F. and Sugden D. (2005) Cosmogenic ^{3}He concentrations in ancient flood deposits from the Coombs Hills, northern Dry Valleys, East Antarctica: interpreting exposure ages and erosion rates. *Earth Planet. Sci. Lett.* **230**, 163–175.

Martin L., Blard P., Balco G., Lavé J., Delunel R., Lifton N. and Laurent V. (2017) The CREp program and the ICE-D

production rate calibration database: a fully parameterizable and updated online tool to compute cosmic-ray exposure ages. *Quat. Geochronol.* **38**, 25–49.

Masarik J. and Reedy R. C. (1996) Monte Carlo simulation of in-situ-produced cosmogenic nuclides. *Radiocarbon* **38**, 163–164.

McEnroe S. A., Robinson P., Langenhorst F., Frandsen C., Terry M. P. and Boffa Ballaran T. (2007) Magnetization of exsolution intergrowths of hematite and ilmenite: Mineral chemistry, phase relations, and magnetic properties of hemo-ilmenite ores with micron-to nanometer-scale lamellae from Allard Lake, Quebec. *J. Geophys. Res. Solid Earth*, 112.

Nesterenok A. and Yakubovich O. (2016) Production of ^{3}He in rocks by reactions induced by particles of the nuclear-active and muon components of cosmic rays: geological and petrological implications. *Petrology* **24**, 21–34.

Niedermann S. (2002) Cosmic-ray-produced noble gases in terrestrial rocks: dating tools for surface processes. *Rev. Mineral. Geochem.* **47**, 731–784.

Pepin R. O., Palma R. L. and Schlutter D. J. (2001) Noble gases in interplanetary dust particles, II: excess helium-3 in cluster particles and modeling constraints on interplanetary dust particle exposures to cosmic-ray irradiation. *Meteorit. Planet. Sci.* **36**, 1515–1534.

Protin M., Blard P., Marrocchi Y. and Mathon F. (2016) Irreversible adsorption of atmospheric helium on olivine: a lobster pot analogy. *Geochim. Cosmochim. Acta* **179**, 76–88.

Ruszkiczay-Rüdiger Z., Dunai T., Bada G., Fodor L. and Horváth E. (2005) Middle to late Pleistocene uplift rate of the Hungarian Mountain Range at the Danube Bend, (Pannonian Basin) using in situ produced ^{3}He. *Tectonophysics* **410**, 173–187.

Shuster D. L., Farley K. A., Vasconcelos P. M., Balco G., Monteiro H. S., Waltenberg K. and Stone J. O. (2012) Cosmogenic ^{3}He in hematite and goethite from Brazilian "canga" duricrust demonstrates the extreme stability of these surfaces. *Earth Planet. Sci. Lett.* **329**, 41–50.

Stone J. (2000) Air pressure and cosmogenic isotope production. *J. Geophys. Res.* **105**, 23753–23759.

Tauxe L., Luskin C., Selkin P., Gans P. and Calvert A. (2004) Paleomagnetic results from the Snake River Plain: contribution to the time-averaged field global database. *Geochem. Geophys. Geosyst.* **5**.

Trappitsch R., Boehnke P., Stephan T., Telus M., Savina M. R., Pardo O., Davis A. M., Dauphas N., Pellin M. J. and Huss G. R. (2018) New constraints on the abundance of ^{60}Fe in the early solar system. *Astrophys. J. Lett.* **857**, L15.

Trull T. W., Kurz M. and Jenkins W. (1991) Diffusion of cosmogenic ^{3}He in olivine and quartz: implications for surface exposure dating. *Earth Planet. Sci. Lett.* **103**, 241–256.

York D. (1968) Least squares fitting of a straight line with correlated errors. *Earth Planet. Sci. Lett.* **5**, 320–324.

Ziegler J. F., Ziegler M. D. and Biersack J. P. (2010) SRIM–The stopping and range of ions in matter (2010). *Nucl. Instrum. Methods Phys. Res., Sect. B* **268**, 1818–1823.

Associate editor: Anthony Dosseto